catalysts

MDPI

Article

Optimization of Solar Photocatalytic Degradation of Chloroxylenol Using TiO_2, Er^{3+}/TiO_2, and Ni^{2+}/TiO_2 via the Taguchi Orthogonal Array Technique

Ahmed J. Mohammed [1], Abdul Amir H. Kadhum [1], Muneer M. Ba-Abbad [1] and Ahmed A. Al-Amiery [2,*]

[1] Department of Chemical and Process Engineering, Faculty of Engineering and Built Environment, Universiti Kebangsaan Malaysia, Bangi, Selangor 43600, Malaysia; dr.ahmed@eng.ukm.my (A.J.M.); amir8@ukm.edu.my (A.A.H.K.); muneer711@gmail.com (M.M.B.-A.)

[2] Environmental Research Center, University of Technology, Baghdad 10001, Iraq

* Correspondence: 100173@uotechnology.edu.iq; Tel.: +60-3-8921-6406; Fax: +60-3-8911-8345

Academic Editor: Keith Hohn

Received: 22 August 2016; Accepted: 11 October 2016; Published: 20 October 2016

Abstract: In this study, the optical properties of a TiO_2 photocatalyst were enhanced with various impregnations of Er^{3+} and Ni^{2+} separately, using the impregnation method as photocatalysts for the direct solar photolysis degradation of chloroxylenol. The synthesized Er^{3+}/TiO_2 and Ni^{2+}/TiO_2 catalysts were characterized using X-ray diffraction (XRD), field emission scanning electron microscopy (FESEM), energy dispersive X-ray (EDX), metal mapping, and ultraviolet visible (UV–Vis) spectroscopy. The results showed that the Er^{3+}/TiO_2 and Ni^{2+}/TiO_2 nano-particles have the same structures of TiO_2 nano-particles with little difference in particle size. The Er^{3+} and Ni^{2+} ions were well-distributed on the TiO_2 surface, and it was found that the maximum band gap decreased from 3.13 eV for intrinsic TiO_2 to 2.63 eV at 1.8 wt % Er^{3+}/TiO_2 and to 2.47 eV at 0.6 wt % for Ni^{2+}/TiO_2. The initial concentration of chloroxylenol, catalyst loading, and pH of the solution are the most important factors affecting the solar photocatalytic degradation efficiency that were optimized using Design Expert software (version 6.0.10, Minneapolis, MN, USA, 2003). The results showed that the optimal conditions for chloroxylenol degradation include a pH of 4, TiO_2 loading at 3 g/L, and a chloroxylenol concentration of 50 mg/L. These conditions resulted in a degradation efficiency of 90.40% after 60 min of direct solar irradiation, wherein the solar energy recorded during a clear sunny day is 1000 W/m^2. However, some experiments were conducted on a semi-cloudy day to cover all weather stated and to study the degradation kinetics. During semi-cloudy day experiments, using Er^{3+}/TiO_2 and Ni^{2+}/TiO_2 with a solar irradiation activity of 600 W/m^2 for a 60 min exposure at optimal conditions increased the degradation efficiency from 68.28% for intrinsic TiO_2 to 82.38% for Er^{3+}/TiO_2 and 80.70% for Ni^{2+}/TiO_2.

Keywords: photocatalyst; chloroxylenol; photocatalytic degradation; kinetics

1. Introduction

One of the most pervasive problems that people face today is the effluent of toxic compounds in water sources. One of these compounds is chloroxylenol (4-chloro-3,5-dimethylphenol), which is widely used as an antibacterial agent. It is a phenolic derivative used in many product formulations for use as an antiseptic and disinfectant [1]. Chloroxylenol has unique antiseptic properties and is a very effective antimicrobial agent against many germs that cause infections since it disrupts the proton gradient of the cell membrane necessary for the bacteria to produce adenosine triphosphate (ATP). The ATP deficiency results in cell death due to starvation [2]. Chloroxylenol also oxidizes the structure of the cell and impedes the nutrients from passing through the cell wall, causing a loss of normal enzyme

activity leading to cell death. Furthermore, chloroxylenol also changes the permeability of the cell walls of microorganisms and disrupts its biological processes [3]. Owing to its antimicrobial properties, chloroxylenol is widely used in various applications and is present in many products and formulations. Due to the large use of products that contain chloroxylenol in their formulations, it can be discharged directly or via urban sewage systems into aquatic systems. Chloroxylenol, as a biocide, represents a potential hazard and has adverse impacts on human health and the environment [4,5]. Due to this impact, efforts are focused on the removal of this compound from aqueous solutions by coagulation [6], adsorption [7], oxidation [8], and biodegradation [9]. All of these methods have significant limitations and disadvantages. Solar photocatalytic oxidation is a promising method because of the low cost of the energy and most of the pollutants can be completely mineralized to CO_2 with suitable catalysts. TiO_2 is one of the best photocatalysts because it is highly photosensitive, non-toxic, has strong oxidizing power and long-term stability. One of the disadvantages of TiO_2 nano-particles (NPs) is their high band gap energy (3.2 eV). Hence, the doping of TiO_2 NPs with metal (rare earth) ions, wherein these metal ions will become concentrated on the surface of the TiO_2 NPs, is one way to decrease the band gap energy and enhance the photoactivity of the TiO_2 NPs [10]. The absorption of visible light by TiO_2 becomes enhanced because visible light makes up approximately 43% of the solar spectrum as its primary source of energy [11]. However, many researchers have doped TiO_2 with rare earth (RE) and transition metal ions for specific applications in the ultraviolet (UV) and visible frequency ranges [12,13]. A design of experiment (DOE) is an effective method to reduce the total cost of the process by minimizing the number of experimental runs. Many designs, such as the Box–Behnken, Taguchi, D-optimal, and central composite designs, have been used to improve the efficiency of degradation [14]. Recently, the Taguchi method has been reported as the ideal method for the optimization process, which is a simple and easy tool that provides effective solutions [15]. Fewer experimental runs with a higher performance value of the response close to the target value have been obtained by the Taguchi method compared with other methods [16]. To optimize any process using the optimization design, it is necessary to identify all factors that have the highest effect on an existing process. When the Taguchi method is applied, the following two points have to occur: (1) clearly define a set of orthogonal arrays (OA), each of which can be used for many experimental situations; and (2) devise a standard method for the analysis of the results [17–19]. Optimization via the Taguchi method can significantly reduce the time required for experiments, which is used to show the effects of multiple factors on performance and determine which factor has more or less influence on the process [20]. In the Taguchi method, after the generation of the optimum conditions, the experimental results should be confirmed and compared with the prediction results [21]. As a continuation of previous studies [22–28] on nanomaterials and catalysts, herein, we report the solar photocatalytic degradation of chloroxylenol that was optimized by the DOE Taguchi OA using TiO_2 NPs, as well as Er^{3+}/TiO_2 and Ni^{2+}/TiO_2 NPs prepared by the impregnation method.

2. Results and Discussion

2.1. X-ray Diffraction (XRD) of TiO_2, Er^{3+}/TiO_2 and Ni^{2+}/TiO_2 NPs

All prepared samples were subjected to X-ray diffraction (XRD) to investigate the type of crystallinity of the used materials and to determine if any change that occurred during the impregnation of the TiO_2 NPs with Er^{3+} and Ni^{2+} ions. The XRD scanning of the Er^{3+}/TiO_2 and Ni^{2+}/TiO_2 NPs is, respectively presented in Figures 1 and 2. The peaks that appear for both the anatase and rutile types (JCPDS File No. 21-1276) of TiO_2 [29,30] are clear. These patterns show that the structure and phase compositions of the TiO_2 NPs were not affected by impregnation with Er^{3+} and Ni^{2+} ions. Furthermore, the intensity of all TiO_2 peaks decreased, which means that the crystal structure of the TiO_2 NPs is impregnated with Er^{3+} and Ni^{2+} ions.

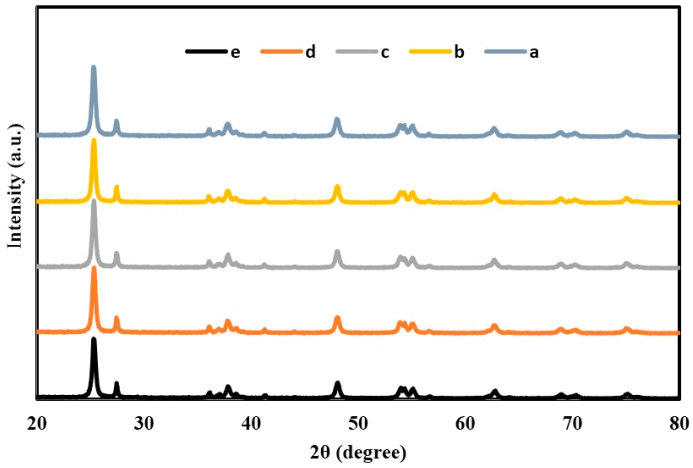

Figure 1. X-ray diffraction pattern: (a) TiO_2; (b) 0.6 wt % Er^{3+}/TiO_2; (c) 1.2 wt % Er^{3+}/TiO_2; (d) 1.8 wt % Er^{3+}/TiO_2; and (e) 2.4 wt % Er^{3+}/TiO_2.

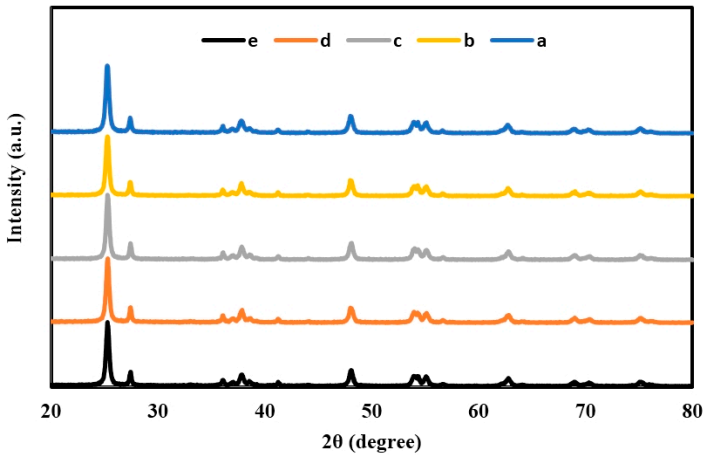

Figure 2. X-ray diffraction pattern: (a) TiO_2; (b) 0.2 wt % Ni^{2+}/TiO_2; (c) 0.4 wt % Ni^{2+}/TiO_2; (d) 0.6 wt % Ni^{2+}/TiO_2; and (e) 0.8 wt % Ni^{2+}/TiO_2.

Tables 1 and 2 show the values of the intensity for each of the peaks. Diffraction spectra of the Er^{3+}/TiO_2 and Ni^{2+}/TiO_2 NPs samples did not indicate the presence of Er or Ni. This result can most likely be attributed to the favorable dispersion of Er^{3+} and Ni^{2+} in the TiO_2 structural lattice [31].

Table 1. Intensity of all peaks of TiO_2 and Er/TiO_2.

2θ	Intensity (Arbitrary Unit, a.u.)				
	TiO_2	0.6 wt % Er/TiO_2	1.2 wt % Er/TiO_2	1.8 wt % Er/TiO_2	2.4 wt % Er/TiO_2
25.2712	2158	1984	1911	1879	1855
27.4136	515	498	493	481	474
37.3038	127	105	100	90	90
48.0908	555	536	481	478	473
53.8206	311	310	288	262	230
53.97	379	368	351	346	336
55.116	367	340	313	291	283
62.7142	292	285	272	249	241
68.8675	165	149	143	131	120
70.2128	145	114	109	108	104
75.0956	185	164	163	151	147

Table 2. Intensity of all peaks of TiO_2 and Ni/TiO_2.

2θ	Intensity (Arbitrary Unit, a.u.)				
	TiO_2	0.2 wt % Ni/TiO_2	0.4 wt % Ni/TiO_2	0.6 wt % Ni/TiO_2	0.8 wt % Ni/TiO_2
25.2712	2158	1964	1922	1866	1834
27.4136	515	504	464	440	410
37.3038	127	110	100	108	108
48.0908	555	536	514	509	483
53.8206	311	284	284	282	270
53.9700	379	348	347	343	316
55.1160	367	334	329	319	294
62.7142	292	254	254	253	242
68.8675	165	144	138	133	108
70.2128	145	122	113	111	106
75.0956	185	178	160	156	141

The catalyst crystallite size D was determined according to Debye–Scherer equation (Equation (1)):

$$D = \frac{K\lambda}{\beta \cos\theta} \quad (1)$$

where K is the Scherer constant (K = 0.89), λ is the incident X-ray wavelength, β is the peak width at half maximum, and θ is the Bragg diffraction angle. The data of the catalyst crystallite size is presented in Table 3 for TiO_2 with several wt % of Er^{3+} and Ni^{2+}. It is observable that there is a small increase in particle size as impregnation increases for Er^{3+}/TiO_2 and Ni^{2+}/TiO_2 samples.

Table 3. Catalyst crystallite size of TiO_2 with several wt % of Er^{3+} and Ni^{2+}.

Sample	Crystallite (nm)
TiO_2	28.72
0.6 wt % Er^{3+}/TiO_2	28.84
1.2 wt % Er^{3+}/TiO_2	31.53
1.8 wt % Er^{3+}/TiO_2	33.93
2.4 wt % Er^{3+}/TiO_2	35.93
0.2 wt % Ni^{2+}/TiO_2	28.98
0.4 wt % Ni^{2+}/TiO_2	30.84
0.6 wt % Ni^{2+}/TiO_2	31.10
0.8 wt % Ni^{2+}/TiO_2	31.51

2.2. Catalyst Surface Morphology of TiO_2, Er^{3+}/TiO_2 and Ni^{2+}/TiO_2 NPs

The morphologies of the Er^{3+}/TiO_2 and Ni^{2+}/TiO_2 NPs were investigated using field emission scanning electron microscopy (FESEM), energy dispersive X-ray (EDX), and metal mapping. The FESEM images are shown in Figure 3. The images revealed that the shape of the particles are mostly spherical, and less agglomeration was observed in the Er^{3+}/TiO_2 sample than the Ni^{2+}/TiO_2 sample.

EDX analysis was conducted on the Er^{3+}/TiO_2 and Ni^{2+}/TiO_2 samples to investigate the presence of Er and Ni on the TiO_2 surface. The results of the EDX spectra are shown in Figure 4 and show that the Er and Ni are present in each of their respective samples. Additionally, the EDX spectral data provided the wt % of the Er and Ni content in the samples, and the results are summarized in Table 4. These results indicate that there is good agreement between the calculated and actual content of Er and Ni. Metal mapping tests were conducted to investigate the dispersion of Er and Ni on the TiO_2 surface. The results are shown in Figure 5 and reveal a good distribution of Er and Ni on the TiO_2 NPs in each of the prepared samples.

Table 4. Calculated and actual wt % of Er and Ni on TiO_2 surface using energy dispersive X-ray (EDX).

Sample	Calculated Metal (wt %)	Actual Metal (wt %) by EDX
0.6 wt % Er^{3+}/TiO_2	0.6	0.72
1.2 wt % Er^{3+}/TiO_2	1.2	1.31
1.8 wt % Er^{3+}/TiO_2	1.8	2.06
2.4 wt % Er^{3+}/TiO_2	2.4	2.45
0.2 wt % Ni^{2+}/TiO_2	0.2	0.16
0.4 wt % Ni^{2+}/TiO_2	0.4	0.31
0.6 wt % Ni^{2+}/TiO_2	0.6	0.59
0.8 wt % Ni^{2+}/TiO_2	0.8	0.74

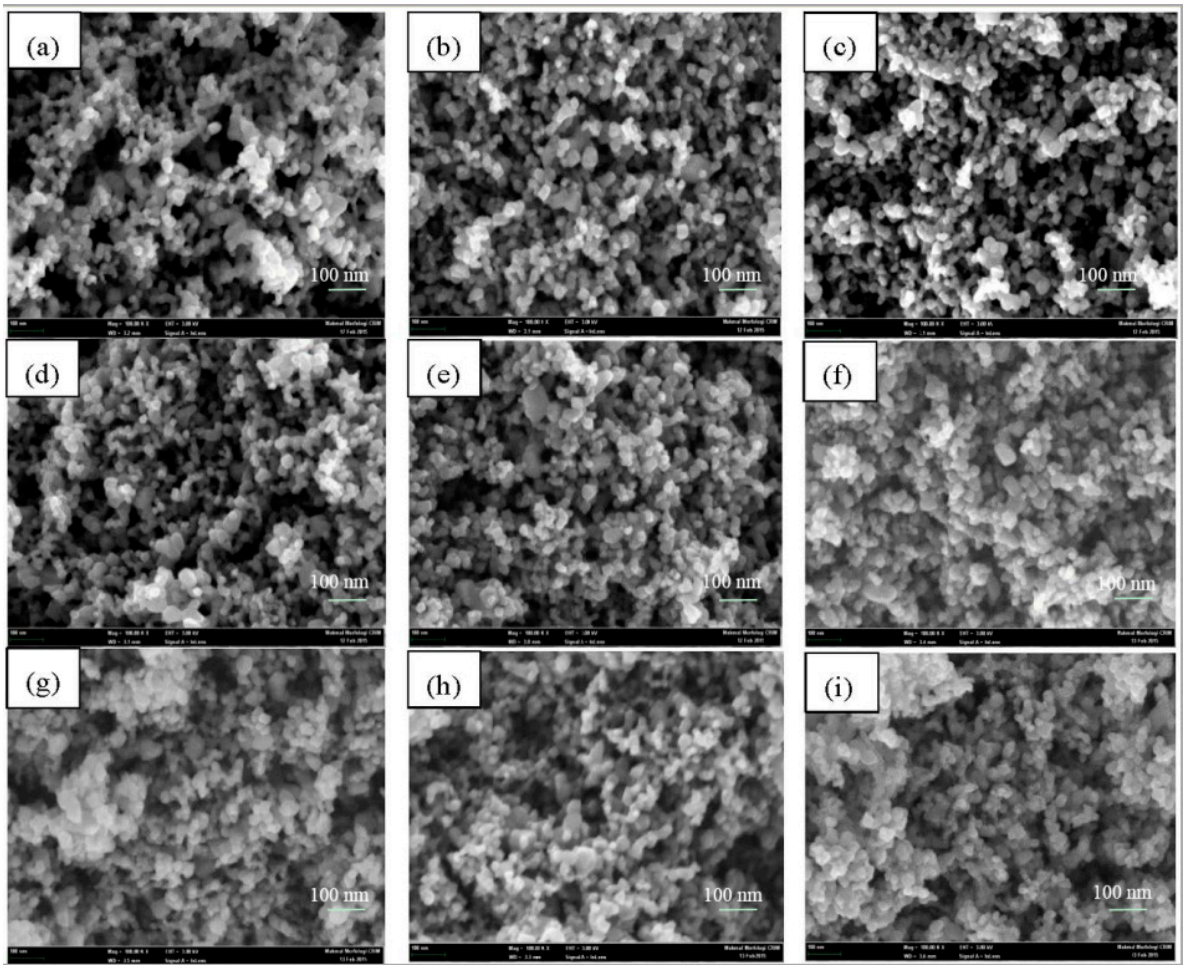

Figure 3. Field emission scanning electron microscopy images: (**a**) TiO_2; (**b**) 0.6 wt % Er^{3+}/TiO_2; (**c**) 1.2 wt % Er^{3+}/TiO_2; (**d**) 1.8 wt % Er^{3+}/TiO_2; (**e**) 2.4 wt % Er^{3+}/TiO_2; (**f**) 0.2 wt % Ni^{2+}/TiO_2; (**g**) 0.4 wt % Ni^{2+}/TiO_2; (**h**) 0.6 wt % Ni^{2+}/TiO_2; and (**i**) 0.8 wt % Ni^{2+}/TiO_2.

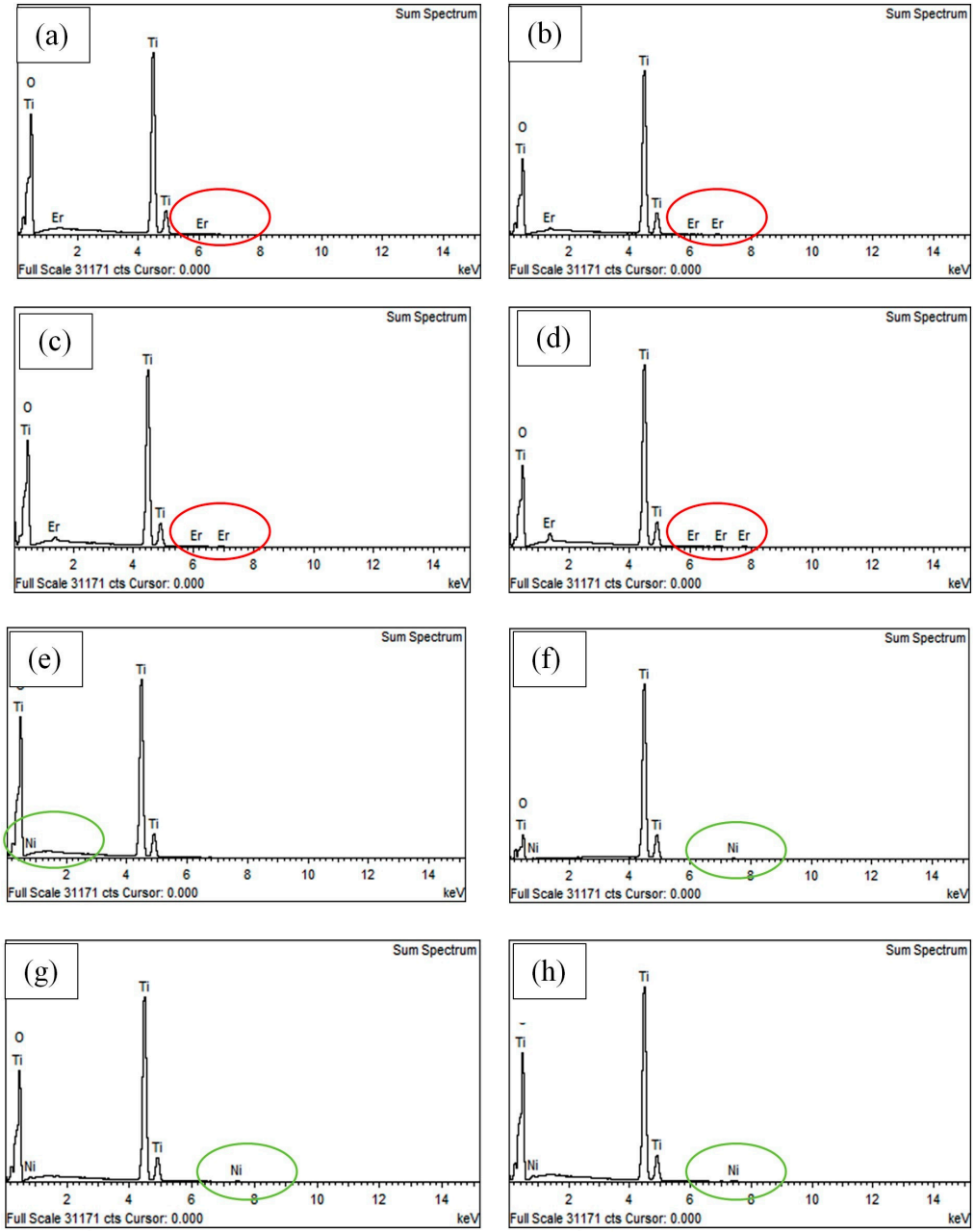

Figure 4. Energy dispersive X-ray spectra: (**a**) 0.6 wt % Er^{3+}/TiO_2; (**b**) 1.2 wt % Er^{3+}/TiO_2; (**c**) 1.8 wt % Er^{3+}/TiO_2; (**d**) 2.4 wt % Er^{3+}/TiO_2; (**e**) 0.2 wt % Ni^{2+}/TiO_2; (**f**) 0.4 wt % Ni^{2+}/TiO_2; (**g**) 0.6 wt % Ni^{2+}/TiO_2; and (**h**) 0.8 wt % Ni^{2+}/TiO_2. Red circle: Er^{3+}; green circle: Ni^{2+}.

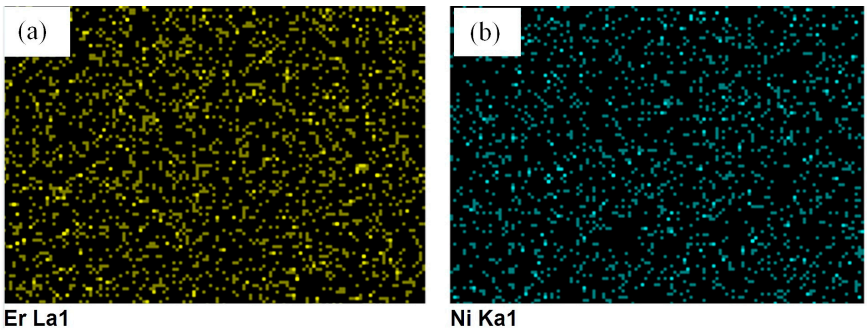

Figure 5. Metal mapping (**a**) Er^{3+}/TiO_2 and (**b**) Ni^{2+}/TiO_2.

2.3. Absorbance and Band Gap of TiO_2, Er^{3+}/TiO_2 and Ni^{2+}/TiO_2 NPs

The absorbance spectra for all the prepared samples (0.6, 1.2, 1.8, and 2.4 wt %) and (0.2, 0.4, 0.6, and 0.8 wt %) of Er^{3+}/TiO_2 and Ni^{2+}/TiO_2, respectively, were recorded at room temperature and are shown in Figure 6. The maximum absorption was observed at 320 nm. The direct band gap (E_g) values of TiO_2, Er^{3+}/TiO_2 and Ni^{2+}/TiO_2 NPs were determined using the following direct transition equation (Equation (2)):

$$\alpha h\upsilon = E_d \left(h\upsilon - E_g\right)^{\frac{1}{2}}. \quad (2)$$

where (α) is the optical absorption coefficient, h is Planck's constant, υ is the frequency ($h\upsilon = 1240/\text{wavelength}$), E_g is the direct band gap, and E_d is a constant [32]. By plotting $(\alpha h\upsilon)^2$ as a function of the photon energy ($h\upsilon$) and extrapolating the linear portion of the curve to a value of zero, band gap (E_g) was calculated and is shown in Figure 7. The obtained values of the band gap (E_g) of TiO_2 with several wt % of Er^{3+} and Ni^{2+} are listed in Table 5. The minimum values of the band gap energies obtained are 2.63 and 2.47 eV for Er^{3+}/TiO_2 and Ni^{2+}/TiO_2 NPs, respectively.

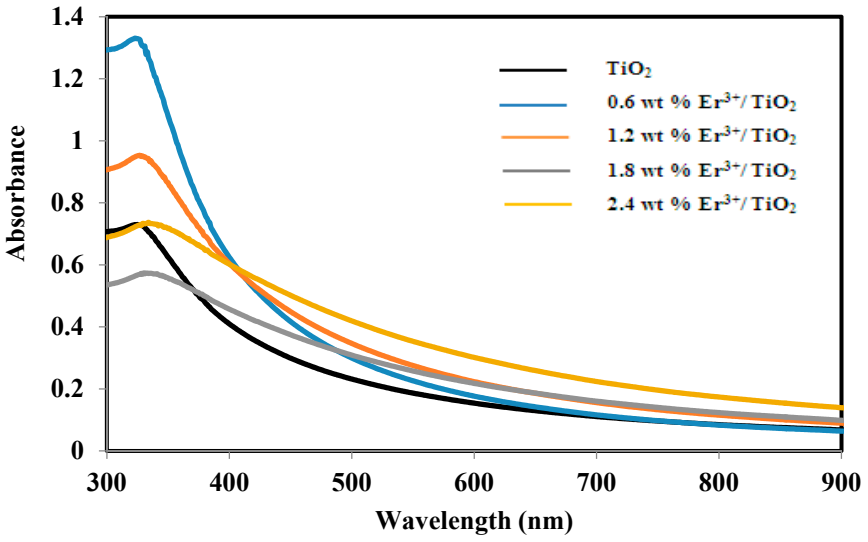

(**a**)

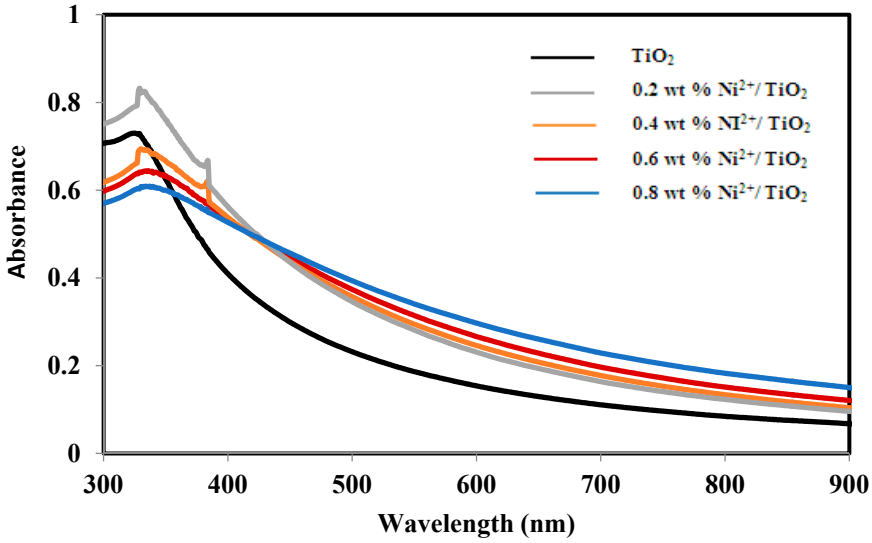

(**b**)

Figure 6. Ultraviolet visible spectra: (**a**) Er^{3+}/TiO_2 nano-particles (NPs) and (**b**) Ni^{2+}/TiO_2 NPs.

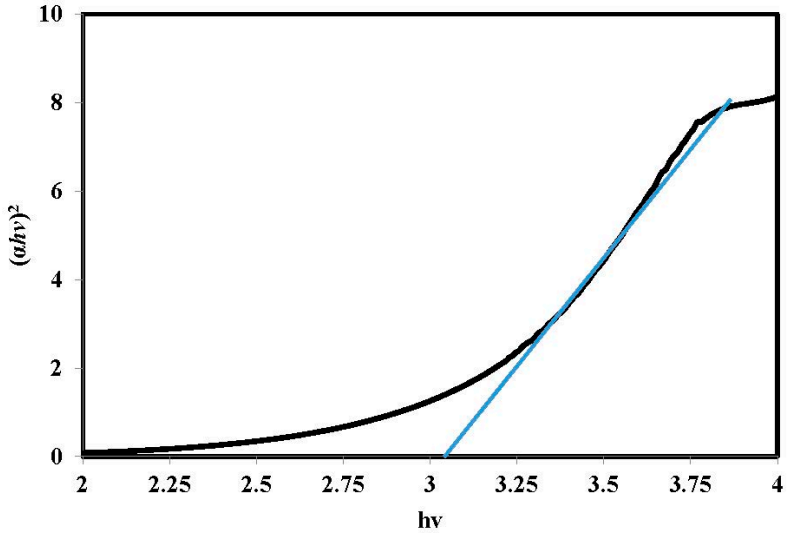

Figure 7. Direct band gap energy (E_g) calculation.

Table 5. Band gap (E_g) of TiO_2 with several wt % of Er^{3+} and Ni^{2+}

Sample	Band Gap Energy (eV)
TiO_2	3.13 ± 0.02
0.6 wt % Er^{3+}/TiO_2	3.20 ± 0.02
1.2 wt % Er^{3+}/TiO_2	3.00 ± 0.02
1.8 wt % Er^{3+}/TiO_2	2.63 ± 0.02
2.4 wt % Er^{3+}/TiO_2	2.70 ± 0.02
0.2 wt % Ni^{2+}/TiO_2	2.60 ± 0.02
0.4 wt % Ni^{2+}/TiO_2	2.50 ± 0.02
0.6 wt % Ni^{2+}/TiO_2	2.47 ± 0.02
0.8 wt % Ni^{2+}/TiO_2	2.61 ± 0.02

2.4. Experimental Design

2.4.1. Response of Solar Photocatalytic Degradation Experiments and Modeling

All experiments were conducted according to the Taguchi OA plan shown in Table 6 under constant direct solar radiation on a clear sunny day. All samples were exposed to solar radiation for a period of 60 min. The degradation efficiency (DE%) was calculated using Equation (1). The results of the DE% for all experiments are listed in Table 6. The results of the predicted values of the DE% generated by the model created by Design Expert software are in agreement with the experimental results presented in Table 6.

Table 6. Actual and predicted values of photocatalytic degradation efficiency percentage (DE%) of chloroxylenol.

Standard	Run Number	A: Catalyst Loading (g/L)	B: pH	C: Concentartion (mg/L)	DE% (Actual)	DE% (Predicted)
1	8	1	4	50	86.75	84.48
2	9	1	6	100	50.12	49.99
3	3	1	8	150	42.9	45.29
4	2	2	4	100	54.55	56.94
5	6	2	6	150	49.65	47.38
6	5	2	8	50	87.69	87.56
7	4	3	4	150	52.31	52.18
8	7	3	6	50	85.1	87.49
9	1	3	8	100	60.13	57.86

After the experimental results of the DE% analysis were obtained, the predicted model of the process was fit with a linear regression, and several factors were determined to have a significant effect on the estimated final model. The linear model of the process and the factors affecting the results and respective coefficients are shown in Equation (3) below:

$$DE\% = +63.25 - 3.32 \times A\,[1] + 0.72 \times A\,[2] + 1.29 \times B\,[1] - 1.62 \times B\,[2] + 23.27 \times C\,[1] - 8.31 \times C\,[2] \quad (3)$$

where DE% represents the degradation efficiency determined by UV–Vis spectroscopy; A, B, and C are the catalyst loading, pH, and initial concentration, respectively.

2.4.2. Analysis of Variance (ANOVA)

The ANOVA results are summarized in Table 7. It is clear that the model is significant with a 95% confidence interval since the *p*-value was 0.0371, which is less than 0.05. The analysis revealed that the most significant factor is the initial concentration of the chloroxylenol. The R^2 and R^2_{adj} values, which were 0.9875 and 0.9499, respectively, show that a sufficient model was created to explain the optimization conditions for the degradation process. The adequacy precision was 11.87, which is larger than 4, indicating that the model is adequate.

Table 7. ANOVA analysis results for photocatalytic degradation of chloroxylenol [1].

Source	Sum of Squares	Degree of Freedom	Mean Square	*F*-Value	*p*-Value
Model	2570.93	6	428.49	26.25	0.0371
A	54.95	2	27.48	1.68	0.3722
B	13.22	2	6.61	0.40	0.7120
C	2502.75	2	1251.38	76.66	0.0129
Residual	32.65	2	16.32	–	–

[1] Significant at *p*-value < 0.05, R^2 = 0.9875, R^2_{adj} = 0.9499, Standard Deviation = 4.04, mean = 63.25, Coefficient of Variation = 6.39, press = 660.50, adequacy precision = 11.87. ANOVA, analysis of variance.

The diagnostic plots of the optimization process are shown in Figure 8. The experimental data shows a good fit with the graphical line, confirming that the model provides a good assumption based on the ANOVA results as shown by the normal probability versus the Studentized residual plots in Figure 8a. The random scattering of the experimental points compared to the funnel-shaped pattern that was obtained indicates that the DE% response had an original observation of variance with no problem between the response and the factors, as shown in Figure 8b [33]. Figure 8c shows a good distribution of the experimental points; none were located out of the indicated range. The actual value of the DE% with the predicted value of the model was evaluated by the value of R^2 and R^2_{adj}, as plotted in Figure 8d. All of the points in the figure are close to the line, indicating the capability of the model to predict the optimum conditions for the degradation process. The Studentized residuals for the experimental runs are shown in Figure 8e, which indicates that the model has values less than ± 3.5 for the Studentized residuals, providing a good fit of the model to the response.

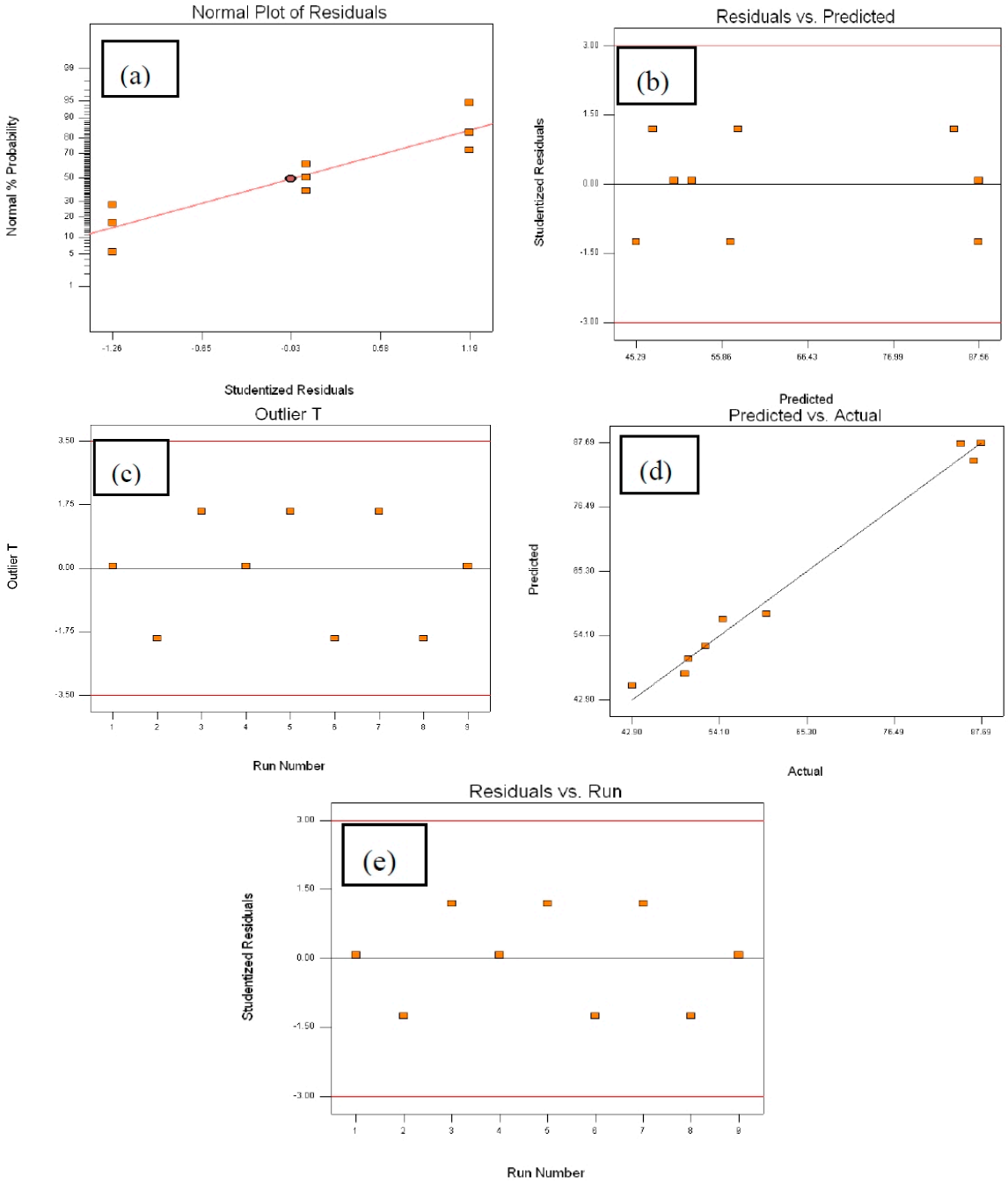

Figure 8. Diagnostic plots of the photocatalytic degradation efficiency percentage (DE%) for the optimization process. (**a**) Studentized residual; (**b**) Residual vs. predicted; (**c**) Outlier; (**d**) Actual vs. predicted; and (**e**) Residual vs. Run.

2.4.3. Optimal Conditions for Maximum DE% and Model Validation

To obtain the optimal conditions of the maximum degradation efficiency, the data shown in Table 6 was optimized numerically using Design Expert software for DE% (larger is better) for the ranges of all factors. The optimal conditions were found to be 3 g/L of Catalyst Loading, pH at 4 and 50 mg/L of chloroxylenol Concentration which the highest DE% of 90.40.

To validate the model shown in Equation (3) created by the software and the optimal conditions for the maximum DE%, three experimental runs were conducted under the optimal conditions listed in Table 8. The results of these experimental runs are shown in Table 8.

Table 8. Results of experimental runs for model validation.

Number of Experiment	Catalyst Loading (g/L)	pH	Concentration (mg/L)	DE%
1	3	4	50	89.57
2	3	4	50	88.21
3	3	4	50	87.67

The average DE% according to the experimental data shown in Table 8 is 88.48%, which is only a 1.92% difference from that of the value predicted by the model (90.40%) and, thus, supports the model validity.

2.5. Kinetics of the Photocatalytic Degradation of Chloroxylenol Using TiO_2 NPs

The experimental results of the photocatalytic degradation of chloroxylenol are shown in Figure 9. The reported results of the photocatalytic degradation of chloroxylenol show that the degradation rates of the photocatalytic oxidation using TiO_2 NPs could be fit with the first-order kinetic model [19]. Figure 10 shows the plot of $\ln(C_0/C)$ vs. the irradiation time for the degradation of chloroxylenol. The linearity of the plot suggests that the photodegradation reaction approximately follows the pseudo-first order kinetics with K = 0.0287 min^{-1}.

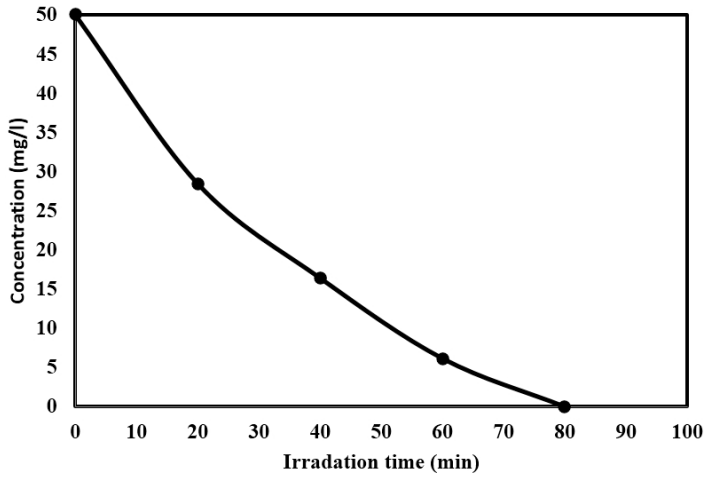

Figure 9. Photocatalytic degradation of chloroxylenol using TiO_2 NPs under optimal conditions.

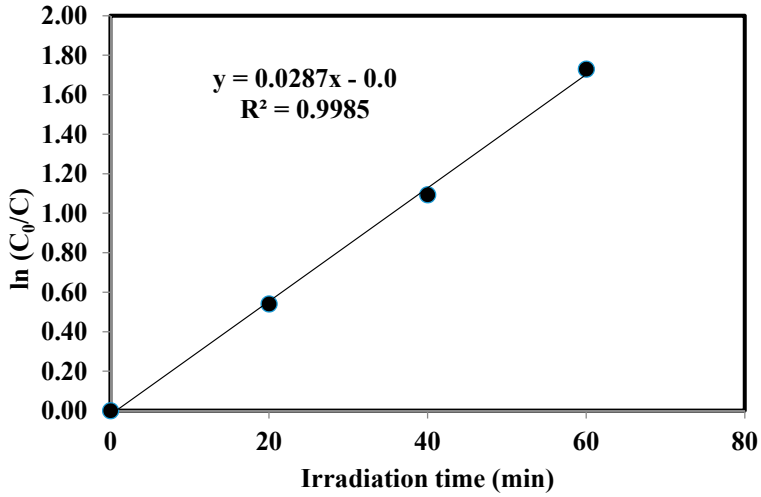

Figure 10. Plot of the pseudo-first order rate constant of photocatalytic degradation of chloroxylenol using TiO_2 NPs under optimal conditions.

Application of Er^{3+}/TiO_2 and Ni^{2+}/TiO_2 NPs in the Photocatalytic Degradation of Chloroxylenol

To investigate the effects of the impregnation of TiO_2 NPs with Er^{3+} and Ni^{2+} on the DE%, experiments were performed using the optimal conditions shown in Table 8 on a semi-cloudy day (solar radiation 600 W/m^2) with a constant reaction time of 60 min using different wt % of Er^{3+}/iO_2 and Ni^{2+}/TiO_2 NPs. The results for the DE% using Er^{3+}/TiO_2 and Ni^{2+}/TiO_2 NPs are shown in Figures 11 and 12, respectively. Figure 11 shows the maximum DE% of 82.38% obtained at a 1.8 wt % of Er^{3+}/TiO_2 provides a 14.10% increase compared with that of the intrinsic TiO_2 NPs at 68.28%. The maximum DE% of 80.70% obtained at a 0.6 wt % of Ni^{2+}/TiO_2 showed an increase of 12.42% compared with that intrinsic TiO_2 NPs, as shown in Figure 12.

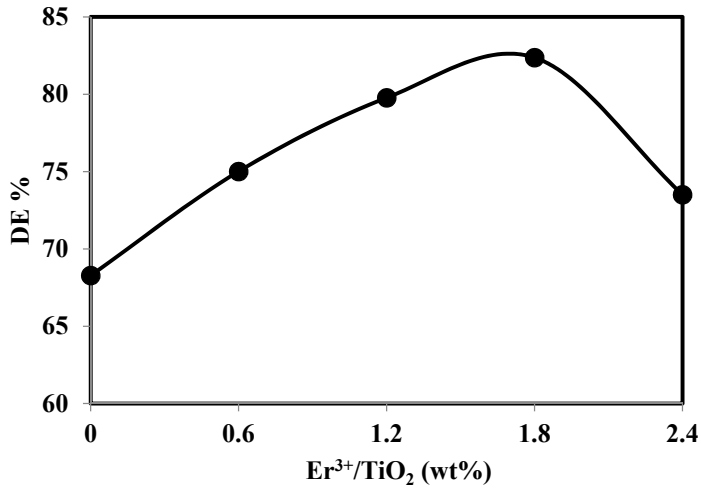

Figure 11. DE% of chloroxylenol using different wt % of Er^{3+}/TiO_2.

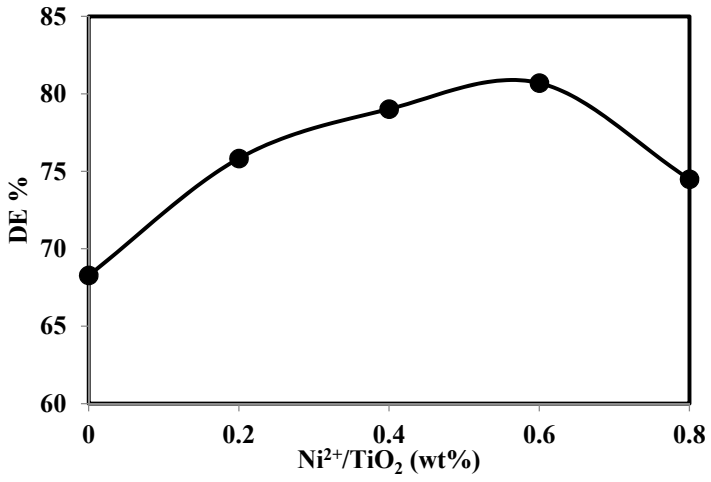

Figure 12. DE% of chloroxylenol using different wt % of Ni^{2+}/TiO_2.

In general, the DE% increased with the increasing concentration of both Er^{3+} and Ni^{2+} relative to the intrinsic TiO_2. The DE% increased up to an optimal concentration for both Er^{3+} and Ni^{2+} over intrinsic TiO_2 at 1.8 and 0.60 wt %, respectively. This result is attributed to the decrease in the band gap because of the shifting absorbance to the visible region. The band gaps of Er^{3+} and Ni^{2+}, compared with intrinsic TiO_2, at 1.8 and 0.60 wt % were found to be 2.63 and 2.47 eV, respectively. These results were compared to intrinsic TiO_2 at 3.13 eV in Table 5. This shifting is attributed to the incorporation of Er^{3+} and Ni^{2+} into the surface of the TiO_2 nanoparticles [34]. After the optimal doping concentrations of Er^{3+} and Ni^{2+} for TiO_2, a decrease in the DE% was observed, which is attributed to the excess Er^{3+}

and Ni^{2+} ions working as a recombination center within the degradation process [35]. However, the electron-hole recombination is faster in the presence of Er^{3+} and Ni^{2+} ions due to the unstable Er^{4+} and Ni^{3+} ions that can easily transfer electrons to the oxygen molecules [36].

3. Materials and Methods

3.1. Materials

All chemicals were purchased from Sigma Aldrich (St. Louis, MO, USA), including erbium (III) acetylacetonate hydrate, CAS grade, 97% purity; nickel (II) acetate tetrahydrate, 98% purity; 99.5% titanium oxide nano-powder (P25) with a diameter of 21 nm using transmission electron microscope TEM, (Philips, Eindhoven, The Netherlands); and chloroxylenol, 98% purity. All chemicals were used without further purification. Deionized water was used for the preparation of the chloroxylenol standard solution, as well as for dilutions.

3.2. Preparation of Er^{3+}/TiO_2 and Ni^{2+}/TiO_2 NPs

To impregnate the TiO_2 NPs with Er^{3+} and Ni^{2+} ions in different wt % of Er/TiO_2 (0.6, 1.2, 1.8, and 2.4 wt %) and Ni/TiO_2 (0.2, 0.4, 0.6, and 0.8 wt %), an 80-mL glass beaker was used. In total, 3 g TiO_2 powder was placed in the beaker. Particular amounts (60, 120, 180, and 240 mg) of erbium (III) acetylacetonate hydrate or nickel (II) acetate tetrahydrate were dissolved in 10 mL of deionized water and sonicated for 10 min. These solutions were then added to the TiO_2 powder dropwise under well-mixing conditions with a glass rod. The mixture was then stirred at 1300 rpm for 2 h, and the mixture was dried overnight at 80 °C, then calcined at 500 °C for 2 h.

3.3. Characterization of Er^{3+}/TiO_2 and Ni^{2+}/TiO_2 NPs

The crystallite size and phase composition of the Er^{3+}/TiO_2 and Ni^{2+}/TiO_2 NPs samples were determined using X-ray diffractometer (XRD) model D8 Advance Bruker AXS X-ray (Bruker, Karlsruhe, Germany) with Cu Kα radiation (1.5406 Å) in a 2θ scan range of 20°–80°.The morphology of the Er^{3+}/TiO_2 and Ni^{2+}/TiO_2 NPs was investigated using a field emission scanning electron microscope, model SUPRA 55 VP (Carl Zesis AG, Munich, Germany), under high resolution, supplied with the energy dispersive X-ray analysis (EDX) system and metal mapping model OXFORD INCA Penta FETx3 (Carl Zesis AG). The zeta potential of the Er^{3+}/TiO_2 and Ni^{2+}/TiO_2 NPs was measured using a Malvern Zeta sizer, model Nano-ZS (Malvern instruments Inc. Worcestershire, UK). A Perkin Elmer (lambda35) UV–Vis spectrophotometer (Perkin Elmer, Waltham, MA, USA) equipped with an integrating sphere was used to record the UV–Vis absorption spectra of the Er^{3+}/TiO_2 and Ni^{2+}/TiO_2 NPs. The spectra were recorded at room temperature with a wavelength range of 200–1100 nm.

3.4. Design of Experiment Using Taguchi Orthogonal Array L9 (3^4)

The purpose of using the Taguchi Orthogonal Array design of experiment is to determine the optimum process conditions to obtain the maximum degradation efficiency (DE%) of chloroxylenol with the minimum number of experiments. In this study, Design Expert software version 6.0.10 was used. Three factors affecting the degradation efficiency of the chloroxylenol were investigated at three levels, as shown in Table 9.

Table 9. Factors and their levels.

Independent Variable	Factor	Level		
		−1	0	+1
Catalyst loading	A	1	2	3
pH	B	4	6	8
Initial concentration	C	50	100	150

The orthogonal array L9 (3^4) experimental design method was chosen to determine the experimental plan as given in Table 10.

Table 10. Experimental plan using the L9 (3^4) orthogonal array.

Standard	Run Number	A: Catalyst Loading (g/L)	B: pH	C: Concentration (mg/L)
1	8	1	4	50
2	9	1	6	100
3	3	1	8	150
4	2	2	4	100
5	6	2	6	150
6	5	2	8	50
7	4	3	4	150
8	7	3	6	50
9	1	3	8	100

3.5. Photocatalytic Reactor and Experimental Procedures

A glass cylindrical slurry batch reactor with a 6.5-cm diameter, 3.8-cm height, 125-mL volume, and a 110-cm^2 radiation area was used to conduct the experiments of solar photocatalytic degradation of chloroxylenol. A 100-mL aqueous solution of a known concentration of chloroxylenol was mixed in the dark with a certain amount of TiO_2 NPs for 60 min to achieve adsorption-desorption equilibrium. The pH was adjusted using HCl and NaOH according to the experimental plan shown in Table 10. Most of the photocatalytic experiments were carried out under similar conditions on clear sunny days from 11:00 am to 2:00 pm with the ambient temperature between 28 and 40 °C, with the exception of those conducted to study kinetics that were run during semi-cloudy days. In each experiment, a sample was withdrawn every 15 min, centrifuged, and then filtered using a 0.22 µm filter to remove the catalyst particles prior to analysis.

3.6. Analytical Method

The UV–Vis spectrophotometer equipped with an integrating sphere was used to determine the concentration of chloroxylenol at λ = 297 nm. Five standard concentrations of chloroxylenol, 12.5, 25, 50, 100 and 150 mg/L, were used to determine the calibration curve. The calibration curve was defined by plotting the concentration versus its absorbance for the five standard concentrations. Then, the absorbance values of the chloroxylenol sample before and after degradation were recorded and compared with the calibration curve to determine their concentrations. The photocatalytic degradation efficiency (DE%) was calculated using the following Equation (4):

$$DE\% = \frac{(C_0 - C)}{C_0}\, x \tag{4}$$

where C_0 is the initial concentration and C is the concentration of the chloroxylenol at different time intervals.

4. Conclusions

The TiO_2 nanoparticles were impregnated with various wt % of erbium and nickel ions using the impregnation method followed by calcination at 500 °C. The Er^{3+} and Ni^{2+} impregnated TiO_2 samples indicated that the band gap energy decreases as the wt % values of the Er^{3+} and Ni^{2+} increase up to 1.8 wt % for the Er^{3+}/TiO_2 and 0.6 wt % for the Ni^{2+}/TiO_2. Agglomeration and particle sizes increased as the ions' wt % increased. The use of Design Expert software and the Taguchi OA method decreased the number of experiments required to predict the optimal conditions. The optimal conditions for solar photocatalytic degradation of chloroxylenol in an aqueous solution include a pH of 4, a TiO_2 loading of 3 g/L, and a concentration of 50 mg/L. The photocatalytic activity of TiO_2 showed obvious

enhancements with only a small wt % increase upon impregnation with Er^{3+} and Ni^{2+} ions. This result was attributed to the decrease in the band gap energy. As a result, there is significant enhancement in the DE% of chloroxylenol by using the impregnated Er^{3+}/TiO_2 and Ni^{2+}/TiO_2.

Acknowledgments: The authors are thankful to the Universiti Kebangsaan Malaysia for the financial support. Also authors would like to thank CRIM (Center for Research and Instrumentation Management UKM).

Author Contributions: Ahmed J. Mohammed did all the experiment as part of his project. Muneer M. Ba-Abbad helped in characterization of the nonmaterial. Abdul Amir H. Kadhum is the principle investigator while Ahmed A. Al-Amiery is a co-investigator. All authors are aware of this manuscript and have agreed to its publication.

Conflicts of Interest: The authors declare no conflict of interest.

References

1. Bruch, M.K. Chloroxylenol: An old–new antimicrobial. In *Handbook of Disinfectants and Antiseptics*; Marcel Dekker: New York, NY, USA, 1996; pp. 265–294.
2. Wilson, M.; Mowad, C. Chloroxylenol. *Dermatitis* **2007**, *18*, 120–121. [PubMed]
3. Kim, B.; Anderson, J.; Mueller, S.; Gaines, W.; Kendall, A. Literature review-efficacy of various disinfectants against Legionella in water systems. *Water Res.* **2002**, *36*, 4433–4444. [CrossRef]
4. Yamano, T.; Shimizu, M.; Noda, T. Allergenicity evaluation of Bioban CS-1135 in experimental animals. *Contact Dermat.* **2004**, *50*, 339–343. [CrossRef] [PubMed]
5. Kupper, T.; Plagellat, C.; Brändli, R.; de Alencastro, L.F.; Grandjean, D.; Tarradellas, J. Fate and removal of polycyclic musks, UV filters and biocides during wastewater treatment. *Water Res.* **2006**, *40*, 2603–2612. [CrossRef] [PubMed]
6. Zhang, G.; Liu, Z.; Song, L.; Hu, J.; Ong, S.; Ng, W. Post-treatment of banknote printing works wastewater ultrafiltration concentrate. *Water Res.* **2004**, *38*, 3587–3595. [CrossRef] [PubMed]
7. Kestioglu, K.; Yonar, T.; Azbar, N. Feasibility of physico-chemical treatment and advanced oxidation processes (AOPs) as a means of pretreatment of olive mill effluent (OME). *Process Biochem.* **2005**, *40*, 2409–2416. [CrossRef]
8. Song, S.; Liu, Z.; He, Z.; Li, Y.; Chen, J.; Li, C. Degradation of the biocide 4-chloro-3, 5-dimethylphenol in aqueous medium with ozone in combination with ultraviolet irradiation: Operating conditions influence and mechanism. *Chemosphere* **2009**, *77*, 1043–1051. [CrossRef] [PubMed]
9. Ghanem, K.M.; Al-Fassi, F.A.; Al-Hazmi, N.M. Optimization of chloroxylenol degradation by Aspergillus niger using Plackett-Burman design and response surface methodology. *Rom. Biotechnol. Lett.* **2013**, *18*, 7983–7994.
10. Ibhadon, A.O.; Fitzpatrick, P. Heterogeneous photocatalysis: Recent advances and applications. *Catalysts* **2013**, *3*, 189–218. [CrossRef]
11. Estrellan, C.R.; Salim, C.; Hinode, H. Photocatalytic activity of sol–gel derived TiO_2 Co-doped with iron and niobium. *React. Kinet. Catal. Lett.* **2009**, *98*, 187–192. [CrossRef]
12. Yu, C.L.; Yang, K.; Yu, J.; Peng, P.; Cao, F.; Li, X.; Zhou, X.C. Effects of rare earth Ce doping on the structure and photocatalytic performance of ZnO. *Acta Phys. Chim. Sin.* **2011**, *27*, 505–512.
13. Minero, C.; Pelizzatti, E.; Sega, M.; Friberg, S.E.; Sjoblom, J. The role of humic substances in photocatalytic degradation of water contaminants. *J. Dispers. Sci. Technol.* **1999**, *20*, 643–661. [CrossRef]
14. Ba-Abbad, M.M.; Kadhum, A.H.; Mohamad, A.B.; Takriff, M.S.; Sopian, K. Optimization of process parameters using D-optimal design for synthesis of ZnO nanoparticles via sol–gel technique. *J. Ind. Eng. Chem.* **2013**, *19*, 99–105. [CrossRef]
15. Ba-Abbad, M.M.; Chai, P.V.; Takriff, M.S.; Benamor, A.; Mohammad, A.W. Optimization of nickel oxide nanoparticle synthesis through the sol–gel method using Box–Behnken design. *Mater. Des.* **2015**, *86*, 948–956. [CrossRef]
16. Chung, T.; Ba-Abbad, M.M.; Mohammad, A.W.; Hairom, N.H.; Benamor, A. Synthesis of minimal-size ZnO nanoparticles through sol–gel method: Taguchi design optimization. *Mater. Des.* **2015**, *87*, 780–787. [CrossRef]
17. Hong, G.B.; Ma, C.M. Photocatalytic degradation of indoor air pollutants by Pt-TiO_2. *J. Nanomater.* **2012**, *2012*, 88–93. [CrossRef]

18. Chong, M.N.; Lei, S.; Jin, B.; Saint, C.; Chow, C.W. Optimisation of an annular photoreactor process for degradation of Congo Red using a newly synthesized titania impregnated kaolinite nano-photocatalyst. *Sep. Purif. Technol.* **2009**, *67*, 355–363. [CrossRef]
19. Nikazar, M.; Farahani, S.J.; Soltani, M.R. Photocatalytic degradation of ethylene dichloride in water using nano TiO_2 supported on clinoptilolite as a photocatalyst. *Adv. Mater. Phys. Chem.* **2013**, *2*, 274–276. [CrossRef]
20. Marandi, R.; Sharif, A.A.M.; Olya, M.E.; Moradi, R. Preparation, characterization of $NiFe_2O_4$ nanoparticles supported on clinoptilolite and optimization of photocatalytic degradation of pollutants in textile wastewater by Taguchi experimental design. *J. Basic. Appl. Sci. Res.* **2013**, *3*, 443–456.
21. Asghar, A.; Raman, A.A.A.; Daud, W.M.A.W. A comparison of central composite design and Taguchi method for optimizing fenton process. *Sci. World J.* **2014**, *2014*, 1–14. [CrossRef] [PubMed]
22. Mohammad, G.; Mohammed, W.; Marzoog, T.R.; Al-Amiery, A.; Kadhumc, A.; Mohamad, A. Green synthesis, antimicrobial and cytotoxic effects of silver nanoparticles using Eucalyptus chapmaniana leaves extract. *Asian Pac. J. Trop. Biomed.* **2013**, *3*, 58–63.
23. Gaaz, T.S.; Sulong, A.B.; Kadhum, A.A.H.K.; Nassir, M.H.; Al-Amiery, A.A. Impact of sulfuric acid treatment of halloysite on physico-chemic property modification. *Materials* **2016**, *9*, 620. [CrossRef]
24. Gaaz, T.S.; Sulong, A.B.; Akhtar, M.N.; Kadhum, A.A.H.; Mohamad, A.B.; Al-Amiery, A.A. Properties and applications of polyvinyl alcohol, halloysite nanotubes and their nanocomposites. *Molecules* **2015**, *20*, 22833–22847. [CrossRef] [PubMed]
25. Wasmi, W.; Al-Amiery, A.; Kadhum, A.; Takriff, M.; Mohamad, A. Synthesis of vanadium pentoxide nanoparticles as catalysts for the ozonation of palm oil. *Ozone Sci. Eng.* **2016**, *38*, 36–41. [CrossRef]
26. Obayes, H.; Al-Gebori, A.; Khazaal, S.; Jarad, A.; Alwan, G.; Al-Amiery, A. Hypothetical design of carbon nanotube materials based on [8] circulene. *J. Nanoelectron. Optoelectron.* **2015**, *10*, 711–716. [CrossRef]
27. Obayes, H.; Al-Amiery, A.; Jaffar, H.; Musa, A.; Kadhum, A.; Mohamad, A. Theoretical study for the preparation of sub-carbon nano tubes from the cyclic polymerization reaction of two molecules from corannulene, coronene and circulene aromatic compounds. *J. Comput. Theor. Nanosci.* **2013**, *10*, 2453–2457. [CrossRef]
28. Wasmi, W.; Al-Amiery, A.; Kadhum, A.; Mohamad, A. Novel approach: Tungsten oxide nanoparticle as a catalyst for malonic acid ester synthesis via ozonolysis. *J. Nanomater.* **2014**, *2014*, 1–7. [CrossRef]
29. Seery, M.K.; George, R.; Floris, P.; Pillai, S.C. Silver doped titanium dioxide nanomaterials for enhanced visible light photocatalysis. *J. Photochem. Photobiol. A* **2007**, *189*, 258–263. [CrossRef]
30. Pillai, S.C.; Periyat, P.; George, R.; McCormack, D.E.; Seery, M.K.; Hayden, H.; Colreavy, J.; Corr, D.; Hinder, S.J. Synthesis of high-temperature stable anatase TiO_2 photocatalyst. *J. Phys. Chem. C* **2007**, *111*, 1605–1611. [CrossRef]
31. Dahl, M.; Liu, Y.; Yin, Y. Composite titanium dioxide nanomaterials. *Chem. Rev.* **2014**, *114*, 9853–9889. [CrossRef] [PubMed]
32. Vijayalakshmi, R.; Rajendran, V. Synthesis and characterization of nano-TiO_2 via different methods. *Arch. Appl. Sci. Res.* **2012**, *4*, 1183–1190.
33. Box, J.G.E.P.; Hunter, S.; Hunter, W.G. *Statistics for Experimenters: Design, Innovation, and Discovery*, 2nd ed.; Wiley Interscience: Hoboken, NJ, USA, 2005.
34. Schleife, A.; Rinke, P.; Bechstedt, F.; Walle, C. Enhanced Optical Absorption Due to Symmetry Breaking in $TiO_{2(1-x)}$ S_{2x} Alloys. *J. Phys. Chem. C* **2013**, *117*, 4189–4193. [CrossRef]
35. Karunakaran, C.; Dhanalakshmi, R. Semiconductor-catalyzed degradation of phenols with sunlight. *Sol. Energy Mater. Sol. Cells* **2008**, *92*, 1315–1321. [CrossRef]
36. Hassan, M.M.; Ahmed, A.S.; Chaman, M.; Khan, W.; Naqvi, A.H.; Azam, A. Structural and frequency dependent dielectric properties of Fe^{3+} doped ZnO nanoparticles. *Mater. Res. Bull.* **2012**, *47*, 3952–3958. [CrossRef]